Nanoscale

This article can be cited before page numbers have been issued, to do this please use: W. Li, M. Zhang, S. Cai, Y. Xin and H. Tian, *Nanoscale*, 2025, DOI: 10.1039/D5NR02216A.

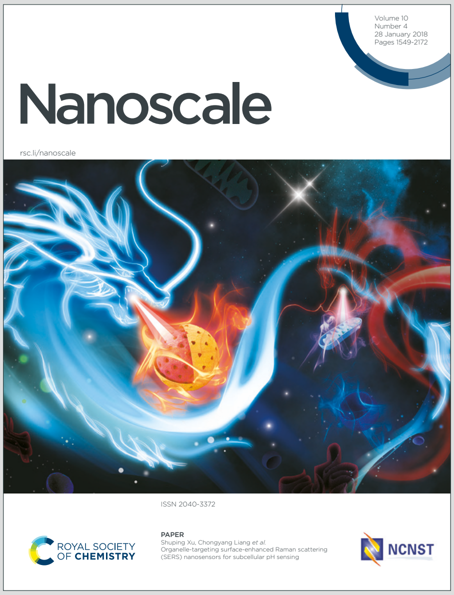

Volume 10
Number 4
28 January 2018
Pages 1549-2172

Nanoscale

rsc.li/nanoscale

ISSN 2040-3372

ROYAL SOCIETY OF CHEMISTRY

PAPER
Shuping Xu, Chongyang Liang *et al.*
Organelle-targeting surface-enhanced Raman scattering (SERS) nanosensors for subcellular pH sensing

NCNST

ROYAL SOCIETY OF CHEMISTRY

rsc.li/nanoscale

View Article Online
DOI: 10.1039/D5NR02216A

A Novel Spherical Mg/Sn Co-doped Alluaudite-type $Na_{2+2x}Fe_{2-x}(SO_4)_3$ Cathode Material for Durable Low-Temperature Sodium-ion Batteries

Weiyi Li, Min Zhang, Shen Cai, Yan Xin, and Huajun Tian[*]

W. Li, M. Zhang, S. C, Y. Xin, H. Tian

Beijing Laboratory of New Energy Storage Technology and Key Laboratory of Power Station Energy Transfer Conversion and System of Ministry of Education, School of Energy Power and Mechanical Engineering,
North China Electric Power University, Beijing, 102206, China
E-mail: Huajun.Tian@ncepu.edu.cn

View Article Online
DOI: 10.1039/D5NR02216A

Abstract

Alluaudite-type $Na_{2+2x}Fe_{2-x}(SO_4)_3$ has been a promising cathode material for sodium-ion batteries (SIBs) due to its high operating voltage and stable structure. However, its actual electrochemical performance suffers from intrinsic sluggish kinetics and poor electronic conductivity. In this work, for the first time, we propose a $Na_{2.48}(Fe_{0.89}Mg_{0.03}Sn_{0.04})_{1.76}(SO_4)_3$ cathode material via Mg/Sn co-doping strategy. Inactive Mg^{2+} stabilizes the structure, while Sn^{4+} inhibits the decomposition of electrolytes under high voltage. The Mg/Sn co-doping strategy enhances the kinetics of sodium ion diffusion reactions, leading to improved electrochemical properties, especially at low temperatures. The optimal NFMS/C-Sn0.03 cathode exhibits a long-term cyclability of remaining 91.6% after 1500 cycles at 5C and outstanding reversible capacity of 74.3 and 58.3 mAh g^{-1} at 10C and even at 50C, respectively. Furthermore, NFMS/C-Sn0.03 cathode demonstrates a high-capacity retention of 95.5% at −5 ℃ and 88.4% at −15 ℃, with a remarkable capacity retention of 93.9% after 1000 cycles at room temperature and 85.5% after 700 cycles at −15 ℃, respectively. The electron paramagnetic resonance (EPR) and atomic force microscopy (AFM) techniques confirmed that the unpaired electronic information and enhanced electronic conductivity could be attributed to the Mg/Sn co-doping. This work provides a feasible approach for designing low-cost, durable, low-temperature, and high-performance cathode materials for SIBs.

Keywords: $Na_{2+2x}Fe_{2-x}(SO_4)_3$, Mg/Sn co-doping, sodium-ion battery, polyanionic cathode material, microsphere

View Article Online
DOI: 10.1039/D5NR02216A

1. Introduction

Energy storage devices, including lithium-ion batteries (LIBs), supercapacitors, flow batteries, compressed air energy storage systems, etc, are the key to the utilization of renewable energy, such as solar, geothermal energy, wind and hydropower, which are intermittent and volatile.[1-4] In the past decade, LIBs have attracted widespread attention owing to their advantages of reliability, long service life, and high energy density.[5-8] Unfortunately, the escalating market demand has exacerbated concerns regarding the rising costs and uneven distribution of lithium resources.[9-12] In response to these challenges, numerous supplements of LIBs have been developed. Notably, sodium-ion batteries (SIBs) are regarded as one of the most promising candidates due to their electrochemical similarities to LIBs, superior wide temperature performance, potential low prices, and huge abundance of Na resources globally.[13-15]

The cathode materials are pivotal factors influencing the energy density, operating voltage, and cost of SIBs.[16-18] Currently, various cathode materials have been proposed and studied extensively, covering polyanionic compounds,[19-21] layered transition metal oxides,[22-24] and Prussian blue analogues.[25, 26] Layered transition metal oxides exhibit high specific capacity and a relatively simple synthesis process. However, the strong O–O and Na–Na electrostatic repulsion during the insertion/extraction of Na^+ ions induces anisotropic lattice displacements and gliding of TMO_2 slabs and Na^+/vacancy rearrangement in NaO_2 slabs, thereby leading to complex phase transitions and electrochemical deterioration.[27] Prussian blue analogues possess acceptable long cycling life, but the challenging issue of crystalline water and low tap density of these materials hinders their practical applications.[28] In contrast, polyanion compounds exhibit comparatively high operational voltage and superior cycling stability, attributed to their intrinsic inductive effect and the stabilizing presence of covalent polyanions in the structure. Among the polyanion materials, iron-based polyanionic compounds emerge as one of the best options, owing to their cost-effectiveness and exceptional abundance of Fe resources [29]

In recent years, various iron-based polyanionic compounds have garnered significant attention, such as $Na_4Fe_3(PO_4)_2P_2O_7$,[29] $Na_2FeP_2O_7$,[30] Na_2FePO_4F,[31] and $Na_{2+2x}Fe_{2-x}(SO_4)_3$ (NFS).[32] Among these cathode materials, alluaudite-type $Na_{2+2x}Fe_{2-x}(SO_4)_3$ exhibits the highest redox potential of ~ 3.8 V (vs. Na^+/Na) and impressive theoretical energy density of 456 Wh kg^{-1} (based on the cathode mass).[32] The framework of NFS is made up of Fe_2O_{10} groups formed by edge-sharing pairs of FeO_6 octahedra and corner-sharing sulphate groups, which offers a potentially long service life. However, the practical electrochemical performance of NFS, especially low-temperature performance, suffer from the poor intrinsic electronic conductivity and inevitable impurity.[33] A few investigations have proved that an

View Article Online
DOI: 10.1039/D5NR02216A

excess amount of sodium sulfate in the precursor mixture, the incorporation of carbon materials, and anion doping can partially address these issues.[34-36] However, the enhancement achieved in NFS remains suboptimal. Currently, the strategy of cation doping has not attracted considerable attention for improving the electrochemical performance of NFS material, especially at low temperature. Furthermore, the underlying mechanisms of such doping strategy are still in the nascent stages of exploration. The quest for effective doping strategies remains a significant challenge.

Herein, for the first time, we successfully designed a Mg/Sn co-doped spherical $Na_{2.48}(Fe_{0.89}Mg_{0.03}Sn_{0.04})_{1.76}(SO_4)_3$ (NFMS/C-Sn0.03) material via a spray-drying approach. The prepared NFMS/C-Sn0.03 cathode exhibits excellent reversible capacity of 71.5 and 58.3 mAh g^{-1} at 10 C and 50 C, respectively, with a long-term cyclability of remaining 91.6% after 1500 cycles at 5 C. Furthermore, NFMS/C-Sn0.03 shows higher discharge-specific capacity than that of NFS/C and NFMS/C at −5 ℃, −15 ℃, and 45 ℃. In particular, NFMS/C-Sn0.03 exhibits satisfactory capacity retention (based on the reversible capacity at room temperature) of 95.5% at −5 ℃ and 88.4% at −15 ℃. The Rietveld X-ray diffraction (XRD) results show that the substitution of Mg and Sn increases the average Na1−O, Na2−O, and Na3−O bond lengths from 2.5669, 2.4670, and 2.7194 Å to 2.5699, 2.5152, and 2.7214 Å, respectively, indicating easier Na^+ ions migration and improved rate performance. The atomic force microscope (AFM) and X-ray photoelectron spectroscopy (XPS) results indicate that the long cycle life of NFMS/C-Sn0.03 cathode could be attributed to the thin and stable CEI film. In summary, this work provides a feasible path to develop cathodes for SIBs with wide-temperature performance, cost-effectiveness, and long-term cycling stability.

2. Experimental section

2.1 Synthesis of NFMS/C-Sn cathode materials

NFS/C, NFMS/C, and NFMS/C-Snx (x=0.01, 0.03, and 0.05) in this study were synthesized using a designed spray-drying and solid-phase synthesis approach. In a typical process, 13.72 mmol of $FeSO_4 \cdot 7H_2O$ (Aladdin, AR, 99%), 20 mmol of Na_2SO_4 (Aladdin, AR, 99%), 0.28 mmol of $MgSO_4 \cdot 7H_2O$ (Aladdin, AR, 99%), and 0.45 g Super P (Hefei Kejing Material Technology Co., Ltd) were distributed in deionized water (Aladdin, AR), referred to as solution A. In addition, 0.15 g ascorbic acid (Aladdin, AR, 99%) was incorporated into solution A to prevent Fe^{2+} from being readily oxidized, referred to as solution B. Solution B was then pumped into a spray dryer to obtain a spherical solid precursor. Finally, the precursor was transferred into a tube furnace (OTF-1200X, Hefei Kejing Material Technology Co., Ltd.), where it underwent treatment under an Ar atmosphere at 350 °C for 24 h. The material obtained by calcination was denoted as NFMS/C. To synthesize Sn-doped NFMS/C,

SnO_2 (Aladdin, AR, 99%) was added in solution B before the spray-drying process. The resulting NFMS/C with different Sn^{4+} contents of 1%, 3%, and 5% were denoted as NFMS/C-Sn0.01, NFMS/C-Sn0.03, and NFMS/C-Sn0.05, respectively.

2.2 Material characterizations

The surface morphological features were obtained using scanning electron microscopy (SEM, Zeiss Sigma 360). The energy dispersive spectrometer (EDS, Oxford EMAX attached to the SEM) was used to confirm the elements and contents in the materials. The microstructures and components of NFS/C, NFMS/C, and NFMS/C-Sn0.03 were further examined by TEM (FEI Tecnai G2 F20). X-ray diffraction (XRD, PANalytical X´Pert3 Powder) analysis was performed using a diffractometer equipped with Cu-Kα radiation ($\lambda = 0.15406$ nm) on the prepared samples to determine the crystal structures with a scanning rate of 2° min^{-1}. Rietveld refinement of XRD was conducted using GSAS. X-ray photoelectron spectroscopy (XPS, Thermo Esca Lab 250Xi) was employed to characterize the surface of the samples. Fourier transform infrared (FTIR, Frontier) spectra were collected in the range of 4000-400 cm^{-1}. The specific surface area of NFS/C, NFMS/C, and NFMS/C-Sn0.03 was conducted by Brunauer-Emmett-Teller (BET) tests. A laser particle size analyzer was used to obtain the particle size distribution. The local electrical conductivity of the sample was tested under a bias of 5 V using atomic force microscopy (AFM, Dimension Icon).

2.3 Cell assembly and electrochemical tests

The CR2032 coin-type cells were produced in an Ar-filled glovebox with O_2 and $H_2O < 0.01$ ppm. The mixture of 80% active material, 10% super P, and 10% poly (vinylidene fluoride) (PVDF) was dissolved in the appropriate amount of N-methyl-2-pyrrolidone (NMP) solvent and milled for 30 min to form a slurry. 80% hard carbon, 10% super P, and 10% PVDF were dissolved in the appropriate amount of NMP to prepare an anode electrode. Subsequently, two kinds of slurry were applied to carbon-coated Al foil and dried overnight at 120 ◦C in an oven, respectively. Na metal foil was used as the negative electrode for the half-cell. The cathode and anode electrodes were punched into disks with a diameter of 12 and 14 mm, respectively. The mass of the active substance of the cathode is about 2 mg cm^{-1}. The electrolyte used was $NaClO_4$ (1 M) in propylene/ethylene carbonate (PC/EC) (1:1 by volume) with 5% fluoroethylene carbonate (FEC) as an additive. A Whatman GF/D was used as a separator. All cells were aged 8 hours before further testing. The cells were tested on a Land battery tester (Land, Wuhan) in the voltage range of 2-4.5 V at 27 ℃. The cells were tested at rates of 0.1 C, 0.5 C, 1 C, 2 C, 5 C, 10 C, 20 C, 30 C, and 50 C (1 C=120 mA g^{-1}) to analyze the rate capability.

View Article Online
DOI: 10.1039/D5NR02216A

Cyclic voltammogram (CV) studies and electrochemical impedance spectroscopy (EIS) were performed on a CHI660a CHI760E electrochemical analyzer (Chenhua Instrument Co. Ltd., Shanghai). Galvanostatic intermittent titration technique (GITT) measurements were conducted at 0.1 C.

3. Results and discussion

The synthetic route and crystal structures of NFS/C, NFMS/C, and NFMS/C-Snx (x=0.01, 0.03, and 0.05) are shown in **Fig. 1**. Fe^{2+}, Na^{+}, Mg^{2+}, SO_4^{2-}, and SnO_2 were uniformly dispersed in a precursor solution using deionized water as a solvent, which was rapidly converted into spherical precursor during the spray-drying process and then sintered into NFS/C, NFMS/C, and NFMS/C-Sn0.03 (details in the experimental section).

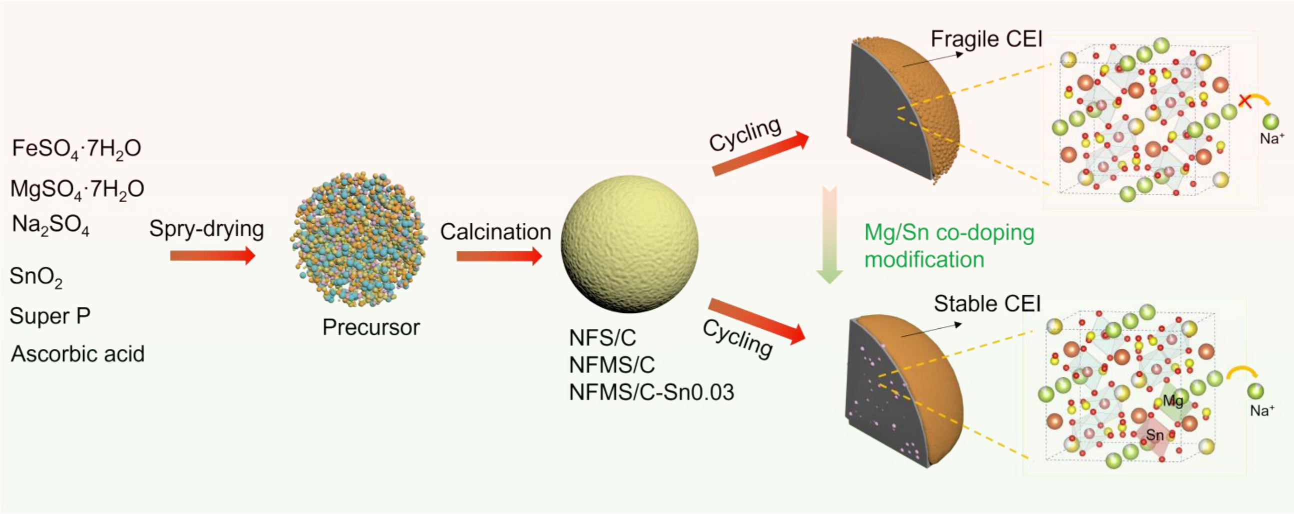

Fig. 1 The schematic diagram of the synthetic route and crystal structure of NFS/C, NFMS/C, and NFMS/C-Sn0.03.

The XRD pattern results of all samples are shown in Fig. S1a. It can be observed that the diffraction peaks of prepared materials are all made of an alluaudite structure (monoclinic phase with C2/c symmetry).[36] The radius of Mg^{2+} ions (0.72 Å) and Sn^{4+} ions (0.69 Å) is close to that of the Fe^{2+} ion (0.78 Å) and much smaller than that of the Na^{+} ion (1.02 Å), facilitating their occupation of iron sites.[37] In the Mg-doped samples, a shift of the characteristic peak near 15.5° (200 crystal plane) to a higher angle is observed, which indicates that Mg is incorporated into the bulk phase with no apparent variations in the NFMS/C peak.[38] However, distinct impurity peaks at about 26.56° and 33.86° in the Mg/Sn co-doped samples are attributed to SnO_2 that is not completely decomposed during calcination. The specific position of Mg^{2+} and Sn^{4+} in the NFS lattice is determined using the following equation[39]:

$$D_{M1(2)}=|(X_M\text{-}X_{M1(2)})\ /\ X_{M1(2)}| + |(r_M\text{-}r_{M1(2)})\ /\ r_{M1(2)}|$$

X_M /$X_{M1(2)}$ and r_M/$r_{M1(2)}$ represent the electronegativity and ionic radius of the dopant (M) and

View Article Online
DOI: 10.1039/D5NR02216A

substitution ion, respectively. Notably, the occupation tendency reverses depending on the D_M values. If D_{M_1} exceeds D_{M_2}, the dopant preferentially occupies M_2 sites due to minimized lattice distortion energy. In contrast, the dopant will be more inclined to occupy the M_1 site under the condition that D_{M_1} is less than D_{M_2}. Through calculation, we found that the D_{Fe} and D_{Na} values for Mg^{2+} doped $Na_{2.48}Fe_{1.76}(SO_4)_3$ are 0.361 and 0.509, respectively, indicating a tendency for Mg to replace Fe sites. For Sn^{4+} doped $Na_{2.48}Fe_{1.76}(SO_4)_3$, the calculated results reveal D_{Fe} is 0.186 and D_{Na} is 1.431, suggesting a driving force for Sn^{4+} to replace Fe sites over Na sites. The detailed crystallographic parameters of NFS/C, NFMS/C, and NFMS/C-Sn0.03 are recorded in Tables S1, S2, and S3. Low error factors in Fig. S1 and **Fig. 2** give reliability to the refinement of XRD data. It is clear that NFMS/C-Sn0.03 exhibits a smaller c value than that of NFS and NFMS/C, indicating a shorter Na^+ diffusion distance. In addition, according to Rietveld refinement results (Table S4), Mg/Sn co-doping plays a positive role in enhancing structural stability and improving sodium ion diffusion kinetics of NFS. The average Na1−O, Na2−O, Na3−O bond lengths of NFMS/C-Sn0.03 is 2.5699, 2.5152, and 2.7214 Å, respectively. However, the average Na1−O, Na2−O, Na3−O bond lengths of NFS/C is only 2.5669, 2.4670, and 2.7194 Å, respectively, indicating that the migration of sodium within NFS lattice is less impeded by oxygen after Mg/Sn co-doping.[38] Furthermore, the average S−O bond length is shortened from 1.4908 to 1.4277 Å after Mg/Sn co-doping, which augments the structural robustness of NFS, thereby facilitating an improvement in its cyclic stability.[40, 41]

The morphology of NFS/C, NFMS/C, NFMS/C-Sn0.01, NFMS/C-Sn0.03, and NFMS/C-Sn0.05 samples were analyzed by SEM (**Fig. 2c** and Fig. S2). The results show that all materials are homogeneous spherical particles. In addition, the EDS maps in **Fig. 2d** and Fig. S3 exhibit a uniform distribution of all elements, which further confirms Mg and Sn incorporation into the NFS lattice interior. A minor accumulation of Sn in some areas of the samples containing Sn is attributed to the incomplete decomposition of SnO_2. The morphology and microstructure of NFS/C, NFMS/C, and NFMS/C-Sn0.03 particles are characterized by TEM, high-resolution TEM (HRTEM), and the corresponding fast Fourier transform (FFT) technique. All particles show typical spherical morphologies with a uniform internal coloration, indicating a solid structure (**Fig. 2e** and Fig. S4).[42] Furthermore, NFS/C, NFMS/C, and NFMS/C-Sn0.03 exhibit well-defined lattice fringes in **Fig. 2f** and Fig. S4, with lattice spacings of 0.2511, 0.2508, and 0.2507 nm, respectively, corresponding to the (42-2) plane. The lattice spacing of the NFMS/C-Sn0.03 sample exhibits a slight reduction compared to that of NFS/C and NFMS/C. This decrease could be ascribed to the partial substitution of Fe sites

View Article Online
DOI: 10.1039/D5NR02216A

by smaller Mg^{2+} ions and Sn^{4+} ions.[43]

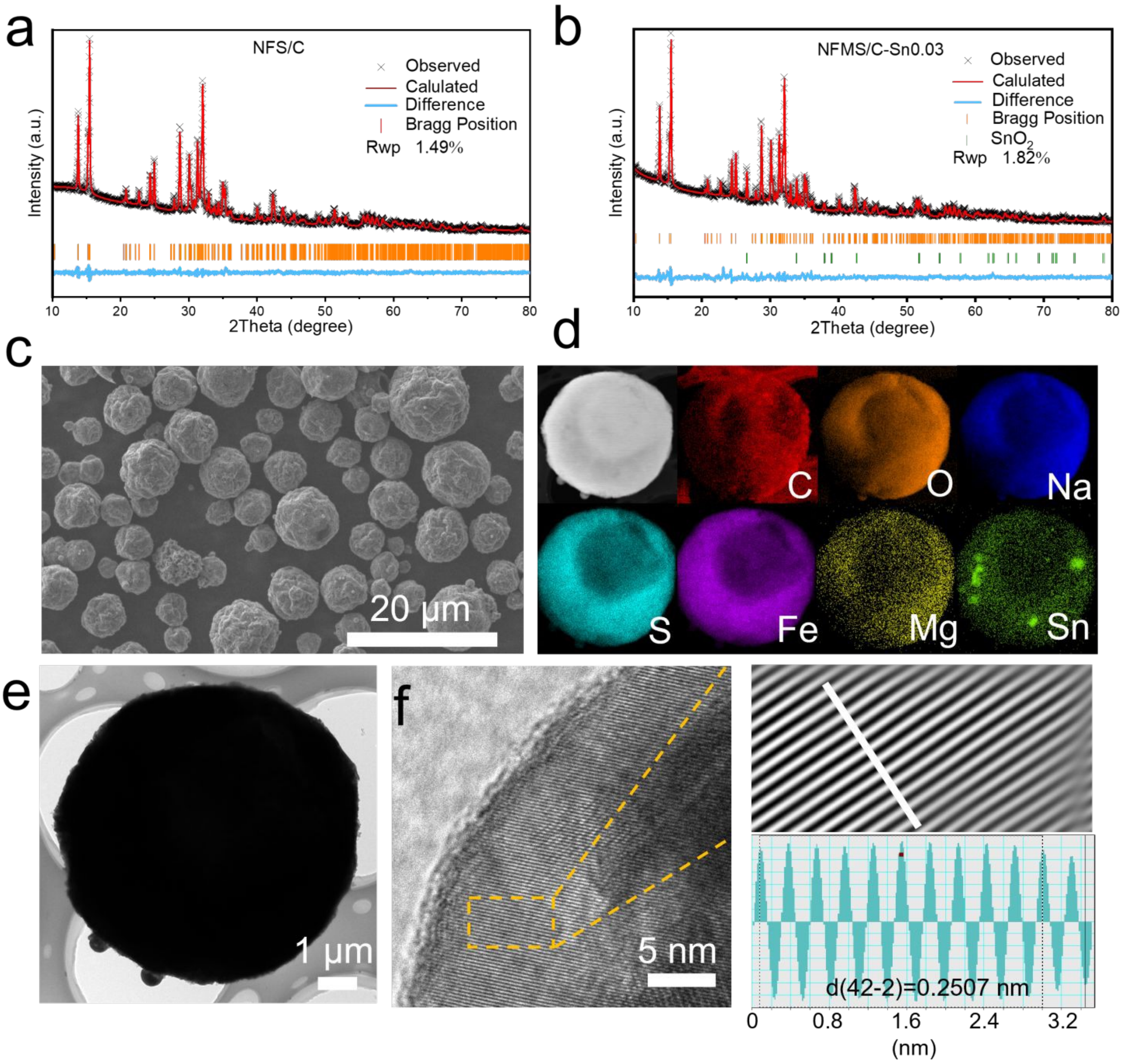

Fig. 2 Structural and morphology characterizations of NFS/C and NFMS/C-Sn0.03 materials. (a and b) XRD and Rietveld plots of NFS/C and NFMS/C-Sn0.03 samples. (c and d) SEM image and TEM-EDS mappings, (e and f) TEM and HRTEM images of NFMS/C-Sn0.03 sample.

The particle size and particle size distribution were ascertained via a laser particle analyzer (**Fig. 3a** and Fig. S5). The D10 and D90 of the NFS/C, NFMS/C, NFMS/C-Sn0.01, NFMS/C-Sn0.03, and NFMS/C-Sn0.05 samples are 5.24, 5.22, 4.95, 4.82, and 4.78 μm, respectively and 18.9, 18.78, 16.77, 16.3, and 16.2 μm, respectively. Noticeably, the Mg/Sn co-doping samples show a smaller particle size than that of NFS/C and NFMS/C, which is attributed to the insoluble SnO_2 in the precursor solution providing additional nucleation sites for the precipitation of the precursor.[42] The BET-specific surface areas and corresponding pore size distributions of NFS/C, NFMS/C, and NFMS/C-Sn0.03 are shown in Fig. S6, **Fig. 3b**, and **Fig. 3c**. The N_2 adsorption/desorption curves of the three samples belong to a well-defined type-Ⅳ isothermal curves.[44, 45] In addition, the specific surface area value of NFMS/C-Sn0.03 (11.70 m^2 g^{-1}) is slightly higher than that of NFS/C (10.79 m^2 g^{-1}) and NFMS/C (10.67 m^2 g^{-1}), which could promote electrolyte penetration.

The structural characteristics of NFS/C, NFMS/C, and NFMS/C-Sn0.03 samples are disclosed by FT-IR spectrometer (**Fig. 3d**). Three samples exhibit stretching vibration of the Fe-O bond, the symmetric/asymmetric variable angular vibration and antisymmetric stretching vibration of the S−O/O−S−O bonding in the SO_4 tetrahedral groups, and stretching vibration of C=C bond in the range of 550-700, 900-1500, and 1550-1650 cm^{-1}, respectively.[46] The broad band at 3500 cm^{-1} is symmetric/ asymmetric stretching of OH^- species, which is related to the exposure of the sample to air before the test.[26] The form of carbon in prepared NFS compounds was studied by Raman spectroscopy (**Fig. 3e**). The characteristic peaks of magnesium and tin were detected in the XPS results of NFMS/C-Sn0.03 (Fig. S7), indicating the success of the Mg/Sn co-doping strategy. The intensity ratios (I_D/I_G) of NFS/C, NFMS/C, and NFMS/C-Sn0.03 are 0.59, 0.61, and 0.56, respectively. In addition, the thermogravimetric analysis (Fig. S8) revealed that NFS/C and NFMS/C-Sn0.03 exhibited a carbon content of 14.9% and 14.5%, respectively, indicating that the amorphous carbon proportion and carbon content of NFS@C and NFMS@C-Sn0.03 are essentially consistent.[47] The electron paramagnetic resonance (EPR) is a powerful tool for accurately detecting the asymmetric electron configuration of the material.[48] In **Fig. 3f**, NFMS/C-Sn0.03 exhibits the most unpaired electronic information, which could contribute to stimulating more active sites and optimizing the electrochemical performance.[21] Furthermore, the visual local electronic conductivity of NFS/C and NFMS/C-Sn0.03 samples was tested by the atomic force microscopy (AFM) technique (PeakForce TUNA). To ensure the reliability of the results, the samples were pressed into thin sheets under a pressure of 20 MPa. The 2D current maps of NFS/C and NFMS/C-Sn0.03 were measured under a bias of 5 V (**Fig. 3g** and **Fig. 3h**).[49] The measured passing current intensity of NFMS/C-Sn0.03 (from 2.9 to 3.2 pA) is significantly higher than that of NFS/C (from 1.1 to 1.4 pA). In addition, the current of the select line (d_1-d_2) of two samples

View Article Online
DOI: 10.1039/D5NR02216A

is shown in **Fig. 3i**. The measured passing current intensity of NFMS/C-Sn0.03 is mostly above 3 pA. On the contrary, the measured passing current intensity of NFS/C is only ~ 1.3 pA. Based on the similar graphitization degree of the carbon in two samples, the enhanced electronic conductivity could be attributed to the Mg/Sn co-doping.

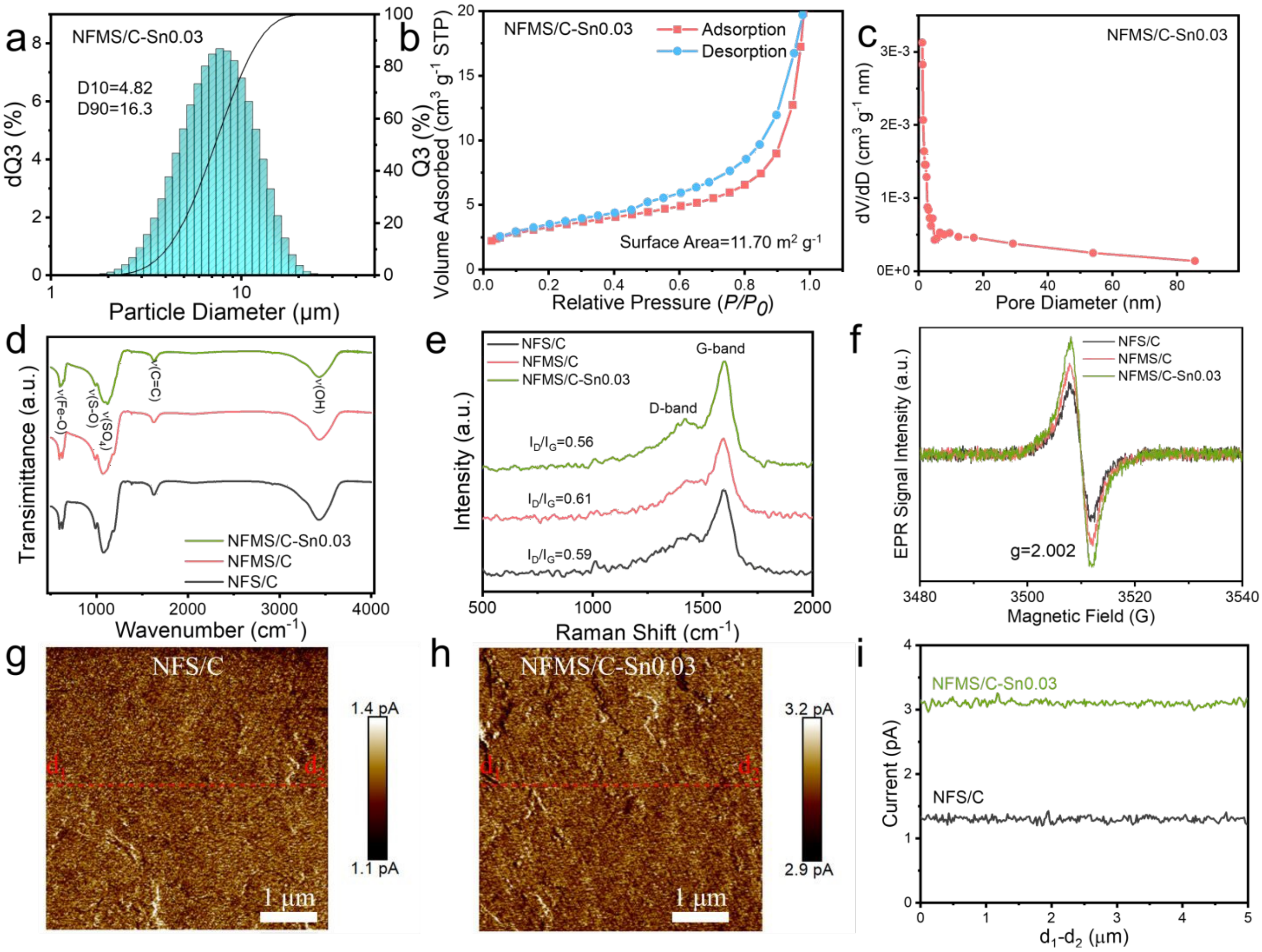

Fig. 3 (a) The particle size distribution image, (b and c) N_2 adsorption/desorption isotherms and aperture distribution curve, (d) FT-IR spectra, (e) Raman spectra, (f) EPR spectra, (g-i) Current maps and PeakForce TUNA current of d_1-d_2 along x-axis of NFS/C, NFMS/C, and NFMS/C-Sn0.03 samples.

The electrochemical performances of NFS/C, NFMS/C, NFMS/C-Sn0.01, NFMS/C-Sn0.03, and NFMS/C-Sn0.05 as cathode electrodes were evaluated using galvanostatic charge-discharge measurements. **Fig. 4a** displays the charging and discharging profiles of all samples at 0.1 C (1 C=120 mAh g^{-1}) within 2-4.5 V.[32] The discharge-specific capacities of five cathodes are 84.3, 83.8, 83.6, 82.0, and 80.5 mAh g^{-1}, respectively. The relatively low initial capacity of doped samples can be attributed to the substitution of Fe^{2+} by the electrochemically inactive Sn^{4+} and Mg^{2+}.[50] **Fig. 4b** exhibits

View Article Online
DOI: 10.1039/D5NR02516A

the rate capability of the NFS/C, NFMS/C, NFMS/C-Sn0.01, NFMS/C-Sn0.03, and NFMS/C-Sn0.05 cathodes at different current rates (0.1, 0.5, 1, 2, 5, 10, 20, 30, and 50 C). The NFS/C cathode shows the highest initial reversible capacity. However, as the current density increases, its discharge-specific capacity declines sharply (only 62.1 mAh g^{-1} at 10 C and 44.2 mAh g^{-1} at 50 C). The Mg-doped cathode (NFMS/C) displays an enhanced reversible capacity of 68.6 mAh g^{-1} at 10 C and 48.9 mAh g^{-1} at 50 C, albeit this enhancement remains insufficient. In accordance with the NFMS/C framework, we incorporated SnO_2 to further elevate the rate performance of NFS, denoting the composites as NFMS/C-Sn0.01, NFMS/C-Sn0.03, and NFMS/C-Sn0.05. Notably, NFMS/C-Sn0.03 cathode exhibits the best capacity retention at each rate than that of NFS/C, NFMS/C, and NFMS/C-Sn0.01, which could be attributed to a smaller Na^+ diffusion distance, with a discharge-specific capacity of 74.3 and 58.3 mAh g^{-1} at 10 C and 50 C, respectively. Upon further increasing the doping level to NFMS/C-Sn0.05, an excessive accumulation of electrochemically inactive Sn occupies the lattice sites of Fe, ultimately resulting in a comparatively lower capacity. Therefore, it is imperative to maintain an optimal concentration of Mg/Sn co-doping. Charge/discharge curves of NFS/C, NFMS/C, NFMS/C-Sn0.01, NFMS/C-Sn0.03, and NFMS/C-Sn0.05 at different current densities exhibit no evidence of severe electrochemical polarization (Fig. S9), indicating that all electrodes prepared by the designed spray-drying approach possess a strong ability to adapt to large current shocks.

Fig. 4c shows the first-cycle CV curves of NFS/C, NFMS/C, and NFMS/C-Sn0.03 electrodes at a scanning rate of 0.1 mV s^{-1} in the voltage window of 2-4.5 V. All electrodes exhibit two pairs of noteworthy redox peaks, which could be attributed to the slow Na^+ diffusion kinetics and structural change of the NFS material in the first cycle.[36] The best reaction kinetics were observed in the NFMS/C-Sn0.03 sample with the lowest polarization. The cycling stability of NFS/C, NFMS/C, NFMS/C-Sn0.01, NFMS/C-Sn0.03, and NFMS/C-Sn0.05 electrodes was tested at 5 C and 10 C (**Fig. 4d-f**). The NFMS/C-Sn0.03 cathode exhibits the highest reversible capacity of 77.5 mAh g^{-1} at 5 C and 75.0 mAh g^{-1} at 10 C, with an excellent capacity retention of 91.6% after 1500 cycles and 88.3% after 2000 cycles, respectively. Moreover, when the mass loading was elevated to ~ 7 mg cm^{-2}, the NFMS @ C-Sn0.03 cathode exhibits a discharge specific capacity of 74.0 mAh g^{-1} at 5 C (Fig. S10). In addition, **Fig. 4g** and Fig. S11 show the electrochemical performance of the materials at low

View Article Online
DOI: 10.1039/D5NR02216A

temperatures. At −5 ℃, the voltage platforms of NFS/C, NFMS/C, and NFMS/C-Sn0.03 cathodes at 0.1 C showed similar performances, with capacity retention (based on the reversible capacity at room temperature) of 77.8%, 80.3%, and 95.5%, respectively. When the temperature drops to −15 ℃, only the NFMS/C-Sn0.03 cathode could remain a distinct voltage platform, with a capacity retention (based on the reversible capacity at room temperature) of 88.4%. By contrast, the capacity retention of NFS/C and NFMS/C cathodes is 30.6% and 56.4%, respectively. Even at 1 C, the NFMS/C-Sn0.03 cathode has a reversible capacity of 70.6 mAh g^{-1} at −5 ℃ and 57.8 mAh g^{-1} at −15 ℃, with a remarkable capacity retention of 93.9% after 1000 cycles and 85.5% after 700 cycles, respectively. The better low-temperature performance of NFMS/C-Sn0.03 could be attributed to the enhanced electrochemical performance of NFMS/C-Sn0.03 cathode with higher Na^+ diffusion coefficient and increased Na−O bond lengths than that of NFS/C and NFMS/C. The outstanding rate performance and remarkable capacity at low temperatures of theNFMS/C-Sn0.03 electrode are superior to those reported for comparable cathode materials (Table S5). Furthermore, at 45 ℃, the NFMS/C-Sn0.03 electrode exhibits higher reversible capacity (78.7 mAh g^{-1}) and better capacity retention (86.7% after 500 cycles at 5 C) than that of the NFS/C and NFMS/C electrodes at the same C-rates (Fig. S12).

View Article Online
DOI: 10.1039/D5NR02216A

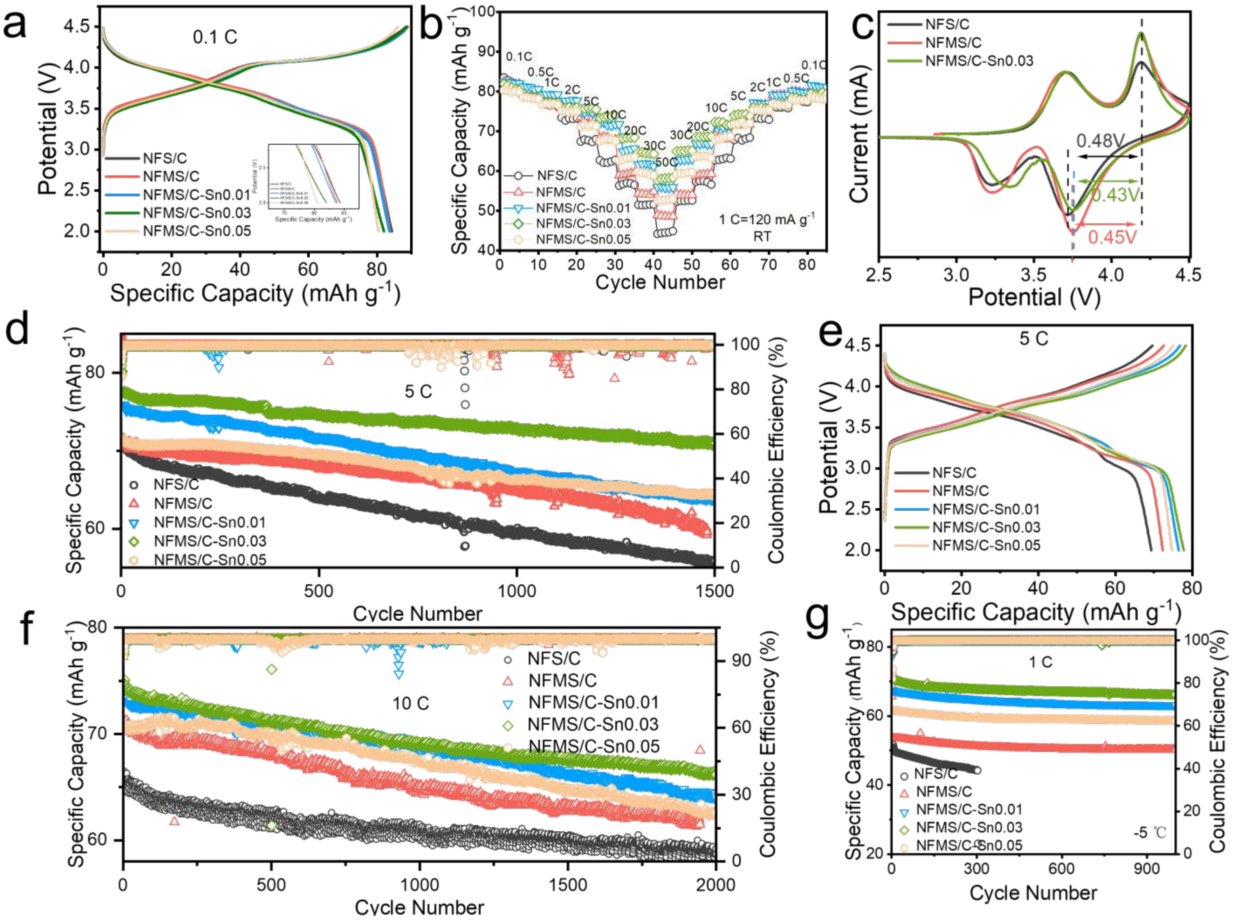

Fig. 4 Electrochemical performance of NFS/C, NFMS/C, NFMS/C-Sn0.01, NFMS/C-Sn0.03, and NFMS/C-Sn0.05. (a) First charge/discharge cycle at 0.1 C, (b) rate performance at different current rates of all samples. (c) CV curves at a scan rate of 0.1 mV s^{-1} in the voltage window of 2-4.5 V of NFS/C, NFMS/C, and NFMS/C-Sn0.03. (d-f) Long cycling stability and charge/discharge curves at 5 C and 10 C, (g) Long cycling stability at 1 C with a low temperature of -5 ℃ of all samples.

To evaluate the beneficial effects of Mg/Sn co-doping on the electrochemical performance of the NFS cathode material, XPS surface analysis was conducted on the cycled NFS/C, NFMS/C, and NFMS/C-Sn0.03 electrodes (Fig. S13). The detail spectrum in the C 1s region of three electrodes (**Fig. 5a)** contains four peaks from Super P, PVDF binder, and decomposition of electrolyte solvent, which can be attributed to C−C (284.8 eV), C−O (286.4 eV), C=O (288.3 eV), and O−C=O (290.5 eV) bonds respectively.[51] **Fig. 5b** shows the high-resolution O 1 s spectrum of three cathodes, which can be fitted to three distinct peaks of Na KLL (536.5 eV), C−O (533.3 eV), and C=O (532.0 eV) bonds.[52] Notably, the signals from C−O (286.4 eV) and C=O (288.3 eV) bonds of NFMS/C-Sn0.03 cathode are weaker than those of NFS/C and NFMS/C cathodes, indicating a thinner CEI film and decreased parasitic reactions between electrolyte and NFMS/C-Sn0.03 cathode.[53-56] The surface roughness and Young's modulus of NFS/C and NFMS/C-Sn0.03 electrodes were tested by AFM (Fig. S14). The arithmetic average roughness (Ra) of the NFMS/C-Sn0.03 electrode is 241 nm, which is smaller than that of NFS/C electrode (316 nm), indicating a more uniform structure. Moreover, Fig. S14c and S14d shows the Young's modulus images of two electrodes. The average modulus of NFMS/C-Sn0.03 electrode is 1.63 GPa, which is significantly higher than that of NFS/C electrode (1.13 GPa). This indicates that NFMS/C-Sn0.03 electrode exhibits higher mechanical strength, which is in accordance with the relatively low abundance of organic species within the CEI layer.[57, 58]

To investigate the kinetic properties of prepared materials, the CV test of NFS/C, NFMS/C, and NFMS/C-Sn0.03 electrodes were executed at scan rates (denoted by v) of 0.1, 0.2, 0.3, 0.4, 0.6, 0.8, and 1.0 mV s^{-1} in the potential window of 2-4.5 V (vs. Na^+/Na). Notably, the cells were pre-scanned at 0.2 mV s^{-1} for three cycles to ensure accuracy. As the scan rate increases, the peak current value (I_p) of the redox peak increases, with the oxidation/reduction peak slightly shifting to a high/low potential (**Fig. 5c** and Fig. S15).[45] **Fig. 5d and c** exhibit linear fitting results of I_p and the square root of the scan rate ($v^{1/2}$), indicating that the redox reaction of three electrodes is a diffusion-dominated process.[59] The following equation explains the relationship between I_p and $v^{1/2}$:

$$I_p = 2.69 \times 10^5 n^{3/2} A D^{1/2} C_{bulk} v^{1/2}$$

where n is the number of electrons involved in the redox process, A is the total electroactive surface area, D and C_{bulk} represent the diffusivity ($cm^2\ s^{-1}$) and concentration (mol cm^{-3}) of the redox active species, respectively, and ν indicates the scan rate during CV tests. The largest slope values corresponding to the redox peaks of NFMS/C-Sn0.03 indicate the higher Na^+ diffusion coefficient and faster reaction kinetics.[60] In addition, GITT is utilized to further understand the effect of Mg/Sn co-doping on Na^+ diffusion kinetics (**Fig. 5f** and Fig. S16). The half-cells were charged/discharged at 0.1 C for 10 min, followed by a relaxation of 30 min to reach a voltage equilibrium (Fig. S17). The calculation equation for Na^+ diffusion coefficients (D_{Na^+}) is as follow:

$$D_{N}{}^{a}{}_{+} = \frac{4}{\pi\tau}\left(\frac{m_B V_B}{M_B S}\right)^2 \left(\frac{\Delta E_S}{\Delta E_\tau}\right)^2 \quad (\tau \ll L^2/D_{Na^+})$$

In the above equation, τ, m_B, V_B, M_B, S, ΔE_S, ΔE_τ, and L are the constant current pulse time, the mass of the active material, molar volume, molecular weight, electrode-electrolyte interface area, the difference between two consecutive stable voltages after relaxation, the total change of cell voltage during a constant current pulse excluding the IR drop, and the thickness of the electrode. As shown in **Fig. 5g**, the D_{Na^+} values of NFMS/C-Sn0.03 are evidently higher than that of NFS/C and NFMS/C, indicating enhanced Na^+ diffusion kinetics.[61] EIS were employed for NFS/C, NFMS/C, and NFMS/C-Sn0.03 cathodes after 500 cycles at 5 C. The Nyquist plots of three cathodes under a fully charged state consist of two deformed semicircles in the high-to-medium frequencies and a sloped line in the low-frequency region (**Fig. 5h**). They can be fitted by the fitting equivalent circuit composed of solution impedance (R_s), conductive interface impedance (R_{sf}), charge transfer impedance (R_{ct}), and Na^+ diffusion impedance in Warburg region (Z_w).[62] Notably, the R_{ct} of the NFMS/C-Sn0.03 sample is 55.8 Ω, which is smaller than that of NFS/C (95.8 Ω) and NFMS/C (67.9 Ω), indicating improved Na^+/e^- charge transfer efficiency.[24] The relationship between Z' and $\omega^{-0.5}$ is displayed in Fig. S18. The smallest σ value for NFMS/C-Sn0.03 indicates the fastest Na^+ diffusion kinetics,[63], which is consistent with the results of CV and GITT.

View Article Online
DOI: 10.1039/D5NR02216A

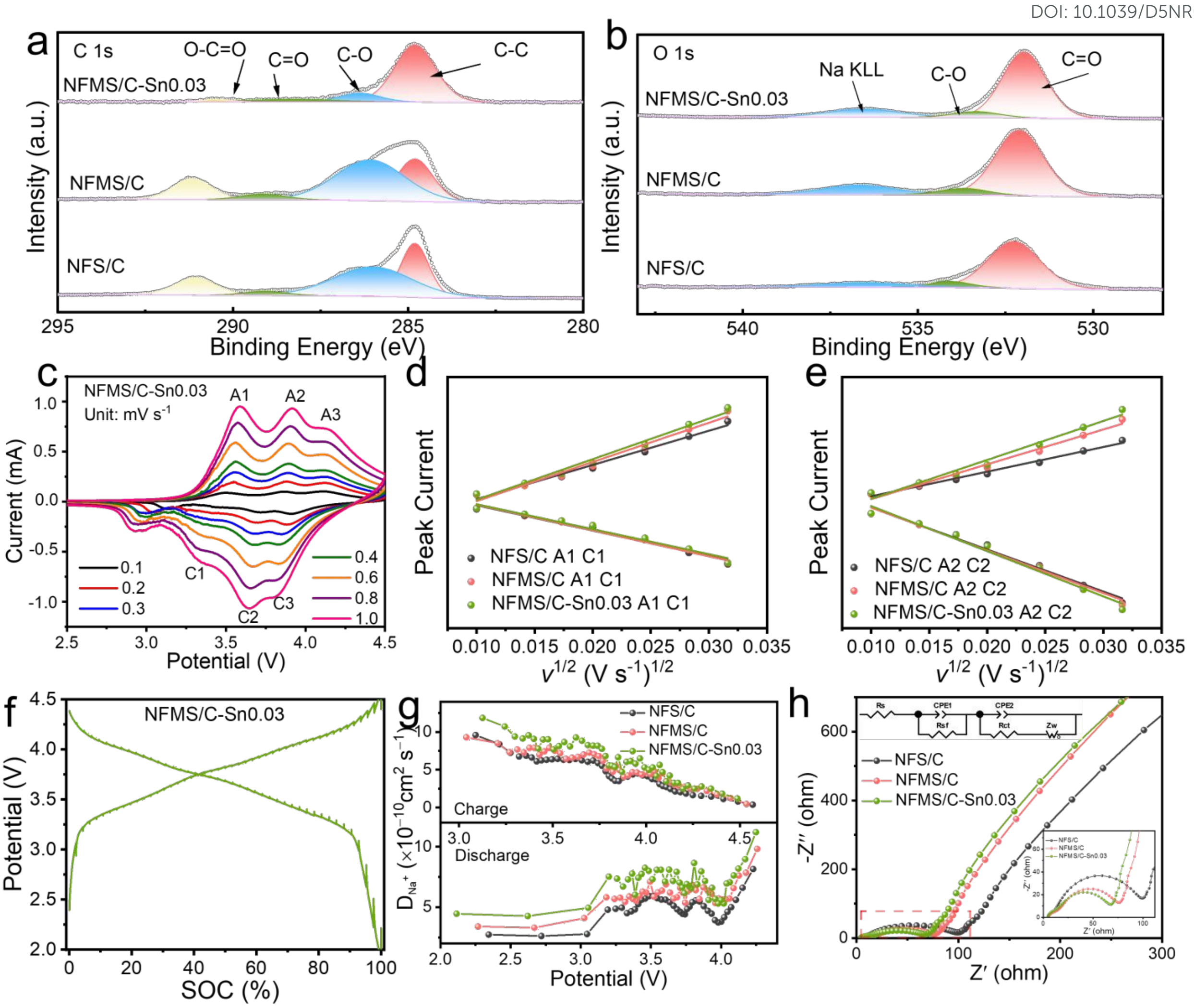

Fig. 5 (a and b) XPS spectra of NFS/C, NFMS/C, and NFMS/C-Sn0.03 electrodes after 3 cycles at 0.1 C. (c-e) CV curves at scan rates of 0.1-1 mV s^{-1} at the voltage window of 2.0-4.5 V (vs. Na$^+$/Na) and linear fitting at the oxidation/reduction peak for CV test, (f) GITT curve at 0.1 C, (g) calculated Na$^+$ diffusion coefficients, (h) EIS test results of NFS/C, NFMS/C, and NFMS/C-Sn0.03 samples.

To evaluate the practical applications for SIBs, we coupled the prepared NFMS/C-Sn0.03 cathode with a commercial hard carbon (HC) anode to assemble a sodium ion full cell (NFMS/C-Sn0.03||HC). The electrochemical evaluation of HC anode in half cell is shown in **Fig. 6a** and Fig. S19. **Fig. 6b and c** exhibit the charge-discharge curves of NFS/C||HC, NFMS/C||HC, and NFMS/C-Sn0.03||HC full cells in the voltage range of 2-4.3 V at 0.1 C and 5 C, respectively. The initial discharge-specific capacity of NFMS/C-Sn0.03||HC is 81.1 mAh g^{-1} at 0.1 C and 76.5 mAh g^{-1} at 5 C, with an average discharge voltage of 3.54 V and 3.46 V, respectively. The rate performance of three full cells is illustrated at the current rates of 0.1, 0.5, 1, 2, 5, 10, 20, 30, and 50 C (**Fig. 6d**). The NFMS/C-Sn0.03||HC full cell

DOI: 10.1039/D5NR02816A

exhibits the best capacity retention at each rate, with a discharge-specific capacity of 71.4 and 59.8 mAh g^{-1} at 10 C and 50 C, respectively. Furthermore, the NFMS/C-Sn0.03||HC full cell could maintain a capacity retention of 89.9% after 4000 cycles and a high energy density of 264.7 Wh kg^{-1} (based on the cathode mass) at 5 C, with an average coulombic efficiency of ~ 99.8% (**Fig. 6e**). The outstanding electrochemical performance achieved in full cells further validates the feasibility of NFMS/C-Sn0.03 as a promising cathode material for SIBs.

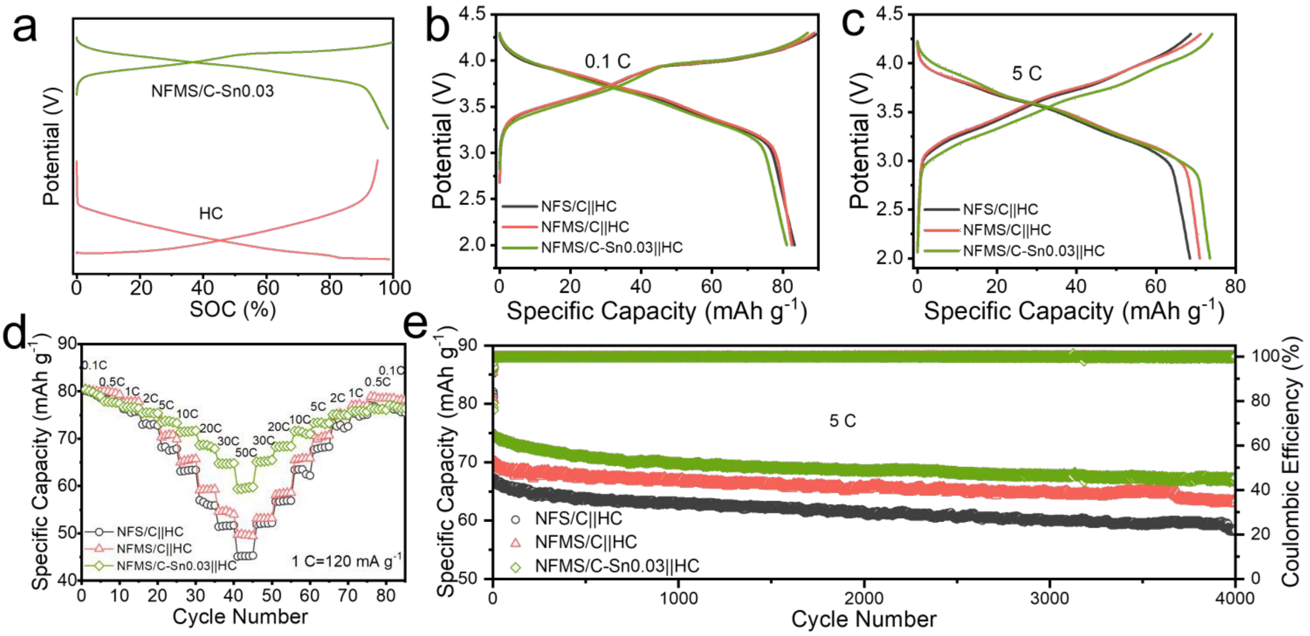

Fig. 6 (a) Charge-discharge curves of HC and NFMS/C-Sn0.03 half-cell. (b and c) Charge-discharge curves of NFS/C||HC, NFMS/C||HC, and NFMS/C-Sn0.03||HC full cells at 0.1 C and 5 C. (d) Rate performance at different current rates, (e) Long cycling stability at 5 C of NFS/C||HC, NFMS/C||HC, and NFMS/C-Sn0.03||HC full cells.

4. Conclusion

In summary, the unique carbon-coated and Mg/Sn co-doped $Na_{2.48}(Fe_{0.89}Mg_{0.03}Sn_{0.04})_{1.76}(SO_4)_3$ was successfully achieved for the modification of NFS cathode materials by a designed spray-drying and solid-phase synthesis approach. The prepared $Na_{2.48}(Fe_{0.89}Mg_{0.03}Sn_{0.04})_{1.76}(SO_4)_3$ (NFMS/C-Sn0.03) cathode exhibits an outstanding discharge-specific capacity of 77.5 at 5 C, with a capacity remaining of 91.6% after 1500 cycles. In addition, the NFMS/C-Sn0.03 cathode could maintain a capacity retention (0.1 C, based on the reversible capacity at room temperature) of 95.5% at −5 ℃ and 88.4% at −15 ℃, with a remarkable capacity retention of 93.9% after 1000 cycles and 85.48% after 700 cycles, respectively. Furthermore, NFMS/C-Sn0.03||HC full cell shows excellent discharge-specific capacity of 81.8 mAh g^{-1} at 0.1 C and remarkable long-cycle stability (capacity retention of 89.9% after 4000 cycles at 5 C). The Rietveld XRD results show that the average S−O bond length of the NFS cathode

View Article Online
DOI: 10.1039/D5NR02216A

decreases after Mg/Sn co-doping, which results in remarkable cycling stability. The GITT and EIS results confirm that the substitution of Mg and Sn could improve the Na^+ diffusion coefficient and electrical conductivity, leading to enhanced rate performance. This work proposes a promising co-doping strategy for achieving practical SIBs with a wide working temperature range.

Acknowledgements

The authors would like to acknowledge the support provided by the Beijing Laboratory of New Energy Storage Technology, North China Electric Power University and the Program of the National Energy Storage Industry-Education Platform, and the Interdisciplinary Innovation Program of North China Electric Power University (No. XM2212315).

Author contributions

H.T., conceived the idea for the project and conducted the project. W.L., M.Z., S.C., and Y.X. wrote the manuscript. M.Z. and S.C. helped W.L. prepare electrode materials and cells in this work. All the authors agreed upon the final version of the manuscript.

Notes

The authors declare no competing financial interest.

References

1. H. Tian, G. Feng, Q. Wang, Z. Li, W. Zhang, M. Lucero, Z. Feng, Z. Wang, Y. Zhang, C. Zhen, M. Gu, X. Shan and Y. Yang, *Nature Communications*, 2022, **13**, 7922.
2. Y. Gao, Q. Yu, H. Yang, J. Zhang and W. Wang, *Advanced Materials*, 2024, **36**, 2405989.
3. H. Zhang, L. Wang and P. Zuo, *Journal of Materials Chemistry A*, 2024, **12**, 30971-31003.
4. Y. Liu, Y. Xin, B. He, F. Zhang, C. Wang and H. Tian, *Advanced Materials*, 2025, **37**, 2417353.
5. Y. Xin, Y. Ge, Z. Li, Q. Zhang and H. Tian, *Acta Physico-Chimica Sinica*, 2024, **40**, 2303060.
6. E. Lee, D. Lee, S. Bessette, S. Park, N. Brodusch, G. Lazaris, H. Kim, R. Malik, R. Gauvin, D. Seo and J. Lee, *Energy & Environmental Science*, 2024, **17**, 3753-3764.
7. X. Zhu, H. Yu, L. Cheng, F. Xu, Z. Wang and L. Fan, *Journal of Materiomics*, 2023, **9**, 82-89.
8. W. Li, B. He, F. Zhang, Y. Xin, S. Cai and H. Tian, *Small*, 2025, **n/a**, 2500271.
9. B. He, F. Zhang, Y. Xin, C. Xu, X. Hu, X. Wu, Y. Yang and H. Tian, *Nature Reviews Chemistry*, 2023, **7**, 826-842.
10. N. Ogihara, K. Nagaya, H. Yamaguchi, Y. Kondo, Y. Yamada, T. Horiba, T. Baba, N. Ohba, S. Komagata, Y. Aoki, H. Kondo, T. Sasaki and S. Okayama, *Joule*, 2024, **8**, 1364-1379.
11. H. Y. Lu, R. L. Hou, S. Y. Chu, H. S. Zhou and S. H. Guo, *Acta Physico-Chimica Sinica*, 2023, **39**, 2211057
12. Z. Xu, X. Hu, B. Fu, K. Khan, J. Wu, T. Li, H. Zhou, Z. Fang and M. Wu, *Journal of Materiomics*, 2023, **9**, 651-660.
13. F. Zhang, B. He, Y. Xin, T. Zhu, Y. Zhang, S. Wang, W. Li, Y. Yang and H. Tian, *Chemical Reviews*, 2024, **124**, 4778-4821.
14. Y. Yu, J. Zhang, R. Gao, D. Wong, K. An, L. Zheng, N. Zhang, C. Schulz and X. Liu, *Energy & Environmental Science*, 2023, **16**, 584-597.
15. R. Chen, D. S. Butenko, S. Li, X. Zhang, G. Li, I. V. Zatovsky and W. Han, *Chinese Chemical Letters*, 2024, **35**, 108358.
16. M. Zhou, X. Zhou, L. Li, X. Chen, Z. Qiao and S. Chou, *Chemical Science*, 2024, **15**, 8651-8663.
17. Y. Guo, R. Jin, M. Fan, W. Wang, S. Xin, L. Wan and Y. Guo, *Chemical Society Reviews*, 2024, **53**, 7828-7874.
18. H. Hou, J. Qiu, B. Li, L. Wang, Z. Zhang, M. Jia, X. Lai, M. Han, P. Yan, D. Liu, D. Dai and B. Wang, *Chinese Chemical Letters*, 2023, **34**, 108810.
19. L. Zhu, S. Xiang, M. Wang, D. Sun, X. Huang, Y. Li, Y. Tang, Z. Peng, Q. Zhang and H. Wang, *Advanced Materials*, 2024, **n/a**, 2408918.
20. T. Li, D. Yang, G. Xu, A. Tang, J. Zheng, X. Zhang, L. Tang, Y. Huang and H. Chen, *Journal of Energy Storage*, 2024, **104**, 114596.
21. Z. Gu, X. Zhao, K. Li, J. Cao, X. Wang, J. Guo, H. Liu, S. Zheng, D. Liu, H. Wu and X. Wu, *Advanced Materials*, 2024, **36**, 2400690.
22. Y. Niu, Z. Hu, H. Mao, L. Zhou, L. Wang, X. Lou, B. Zhang, D. Xiao, Y. Yang, F. Ding, X. Rong, J. Xu, W. Yin, N. Zhang, Z. Li, Y. Lu, B. Hu, J. Lu, J. Li and Y. Hu, *Energy & Environmental Science*, 2024, **17**, 7958-7968.
23. A. Joshi, S. Chakrabarty, S. H. Akella, A. Saha, A. Mukherjee, B. Schmerling, M. Ejgenberg, R. Sharma and M. Noked, *Advanced Materials*, 2023, **35**, 2304440.

24. Y. Huang, Y. Zhang, G. Yuan, D. Ruan, X. Zhang, W. Liu, Z. Zhang and X. Yu, *Applied Surface Science*, 2024, **653**, 159395.
25. C. Tang, W. Lu, Y. Zhang, W. Zhang, C. Cui, P. Liu, L. Han, X. Qian, L. Chen, F. Xu and Y. Mai, *Advanced Materials*, 2024, **36**, 2402005.
26. H. Zhao, Y. Hao, Y. Zhang and Y. Gu, *Journal of Power Sources*, 2025, **630**, 236075.
27. S. Gao, Z. Zhu, H. Fang, K. Feng, J. Zhong, M. Hou, Y. Guo, F. Li, W. Zhang, Z. Ma and F. Li, *Advanced Materials*, 2024, **36**, 2311523.
28. J. Ning, J. Hu, M. Zhou, T. Wang, M. Chen, K. Wang, W. Wang and K. Jiang, *Chemical Engineering Journal*, 2024, **489**, 151531.
29. X. Li, S. Dai, Q. Chen, H. Mao and H. Pan, *Journal of Materials Chemistry A*, 2024, **12**, 29726-29734.
30. H. Kim, R. A. Shakoor, C. Park, S. Y. Lim, J. Kim, Y. N. Jo, W. Cho, K. Miyasaka, R. Kahraman, Y. Jung and J. W. Choi, *Advanced Functional Materials*, 2013, **23**, 1147-1155.
31. Q. Li, Z. Liu, F. Zheng, R. Liu, J. Lee, G. Xu, G. Zhong, X. Hou, R. Fu, Z. Chen, K. Amine, J. Mi, S. Wu, C. P. Grey and Y. Yang, *Angewandte Chemie International Edition*, 2018, **57**, 11918-11923.
32. P. Barpanda, G. Oyama, S. Nishimura, S. Chung and A. Yamada, *Nature Communications*, 2014, **5**, 4358.
33. Y. Liu, Y. Han, Z. Song, W. Song, Z. Miao, Y. Chen, J. Ding and W. Hu, *ACS Applied Materials & Interfaces*, 2024, **16**, 13828-13838.
34. G. Oyama, S. Nishimura, Y. Suzuki, M. Okubo and A. Yamada, *ChemElectroChem*, 2015, 1019.
35. A. Zhao, F. Ji, C. Liu, S. Zhang, K. Chen, W. Chen, X. Feng, F. Zhong, X. Ai, H. Yang, Y. Fang and Y. Cao, *Science Bulletin*, 2023, **68**, 1894-1903.
36. C. Liu, K. Chen, H. Xiong, A. Zhao, H. Zhang, Q. Li, X. Ai, H. Yang, Y. Fang and Y. Cao, *eScience*, 2023, **4**, 100186.
37. Y. Zhang, J. Zhang, T. Shao, X. Li, G. Chen, H. Liu and Z. Ma, *ACS Applied Materials & Interfaces*, 2022, **14**, 14253.
38. Q. Shi, R. Qi, X. Feng, J. Wang, Y. Li, Z. Yao, X. Wang, Q. Li, X. Lu, J. Zhang and Y. Zhao, *Nature Communications*, 2022, **13**, 3205.
39. L. Niu, Z. Liu, G. Liu, M. Li, X. Zong, D. Wang, L. An, D. Qu, X. Sun, X. Wang and Z. Sun, *Nano Research*, 2022, **15**, 3886-3893.
40. X. Qi, Q. Dong, H. Dong, B. Hou, H. Liu, N. Shang, S. Zhang, L. Wang, H. Shao, Y. Shen, S. Chen and X. Zhao, *Energy Storage Materials*, 2024, **73**, 103861.
41. P. Li, M. Gao, D. Wang, Z. Li, Y. Liu, X. Liu, H. Li, Y. Sun, Y. Liu, X. Niu, B. Zhong, Z. Wu and X. Guo, *ACS Applied Materials & Interfaces*, 2023, **15**, 9475-9485.
42. X. Zhang, Z. Huang, Y. Liu, M. Su, K. Li and X. Wu, *Journal of Colloid and Interface Science*, 2023, **650**, 742-751.
43. D. Guo, F. Wang, M. Yang, G. Hu, G. Liu, N. Wu, A. Qin and X. Liu, *Electrochimica Acta*, 2022, **424**, 140695.
44. S. Kadam, R. Kate, U. Chothe, P. Chalwadi, J. Shingare, M. Kulkarni, R. Kalubarme and B. Kale, *ACS Applied Materials & Interfaces*, 2023, **15**, 34651-34661.
45. Y. Xu, L. Yin, C. Yang, Y. Lei, H. Zhang and K. Hui, *ACS Applied Energy Materials*, 2024, **7**,

View Article Online
DOI: 10.1039/D5NR02216A

11890-11899.

46. X. Li, H. Yang, Q. Li, Z. Liu, T. Zhang and G. Liang, *Ionics*, 2024, **31**, 1499-1515.
47. K. Tuo, L. Mao, H. Ding, H. Dong, N. Zhang, X. Fu, J. Huang, W. Liang, S. Li and C. Li, *ACS Applied Energy Materials*, 2021, **4**, 8003-8015.
48. Y. Zhou, G. Xu, J. Lin, Y. Zhang, G. Fang, J. Zhou, X. Cao and S. Liang, *Advanced Materials*, 2023, **35**, 2304428.
49. X. Ge, H. Li, J. Li, C. Guan, X. Wang, L. He, S. Li, Y. Lai and Z. Zhang, *Small*, 2023, **19**, 2302609.
50. H. Fu, Y. Wang, G. Fan, S. Guo, X. Xie, X. Cao, B. Lu, M. Long, J. Zhou and S. Liang, *Chemical Science*, 2022, **13**, 726-736.
51. W. Shi, H. Dong, J. Yin, X. Feng, W. Sun, C. Huang, Y. Cheng and X. Xu, *Journal of Alloys and Compounds*, 2023, **966**, 171530.
52. W. Cheng, J. Ding, Z. Liu, J. Zhang, Q. Liu, X. Wang, L. Wang, Z. Sun, Y. Cheng, Z. Xu, Y. Lei, J. Wang and Y. Huang, *Chemical Engineering Journal*, 2023, **451**, 138678.
53. M. Pan, Y. Wang, Y. Liu, M. Zhang, X. Liu, Y. Yuan, Y. Zhou, W. Liu, T. Chen and K. Liu, *Chemical Engineering Journal*, 2024, **495**, 153396.
54. Q. Zhou, W. Li, D. Ye, W. Wu, S. Qiu, Z. Yin, C. Lu and X. Wu, *Journal of Alloys and Compounds*, 2024, **989**, 174405.
55. J. Shen, H. Li, H. Qi, Z. Lin, Z. Li, C. Zheng, W. Du, H. Chen and S. Zhang, *Journal of Energy Chemistry*, 2024, **88**, 428-436.
56. J. Huang, L. Xu, D. Ye, W. Wu, S. Qiu, Z. Tang and X. Wu, *Journal of Alloys and Compounds*, 2024, **976**, 173397.
57. B. Fu, Y. Su, J. Yu, S. Xie and J. Li, *Electrochimica Acta*, 2019, **303**, 125-132.
58. W. Bian, H. Li, X. Cheng, Z. Zhao, X. Chen and X. Wang, *Journal of Power Sources*, 2025, **630**, 236069.
59. X. Li, Y. Zhang, B. Zhang, K. Qin, H. Liu and Z. Ma, *Journal of Power Sources*, 2022, **521**, 230922.
60. S. Xu, W. Zhu, Y. Yang, Y. Yao, G. Ali, X. Zhang, X. Rui and Y. Yu, *Small Structures*, 2024, **5**, 2300369.
61. L. Shen, Y. Li, C. Hu, Z. Huang, B. Wang, Y. Wang, Q. Liu and F. Ye, *Materials Today Chemistry*, 2023, **30**, 101506.
62. N. Hong, J. Li, H. Wang, X. Hu, B. Zhao, F. Hua, Y. Mei, J. Huang, B. Zhang, W. Jian, J. Gao, Y. Tian, X. Shi, W. Deng, G. Zou, H. Hou, Z. Hu, Z. Long and X. Ji, *Advanced Functional Materials*, 2024, **34**, 2402398.
63. Y. Jin, Y. Li, J. Li, H. Zhou, X. Chen, P. Jiang, Q. Fan, Q. Kuang, Y. Dong and Y. Zhao, *ACS Applied Energy Materials*, 2024, **7**, 4121-4131.

View Article Online
DOI: 10.1039/D5NR02216A

Data Availability Statements

The data supporting this article have been included as part of the Supplementary Information. The data that support the findings of this study are available from the corresponding author upon reasonable request.